PROCEEDINGS OF SPIE

Topological pupil segmentation and point spread function analysis for large aperture imaging systems

Feng, Yi-Ting, Ashcraft, Jaren Nicholas, Breckinridge, James, Harvey, James, Douglas, Ewan, et al.

SPIE.

Topological Pupil Segmentation and Point Spread Function Analysis for Large Aperture Imaging Systems

Yi-Ting Feng[a], Jaren Nicholas Ashcraft[a], James B. Breckinridge[b], James E. Harvey[c], Ewan S. Douglas[d], Heejoo Choi[a, e], Charles Lillie[f], Tony Hull[g], and Dae Wook Kim[*, a, d, e]

[a]James C. Wyant College of Optical Sciences, Univ. of Arizona, Tucson, AZ 85721, USA
[b]California Institute of Technology, Pasadena, CA 91125, USA
[c]Photon Engineering, LLC, Tucson, Arizona 86711, USA
[d]Department of Astronomy & Steward Observatory, Univ. of Arizona, Tucson, AZ 85721, USA
[e]Large Binocular Telescope Observatory, Univ. of Arizona, Tucson, AZ 85721, USA
[f]Lillie Consulting LLC, Playa del Rey, CA 90293, USA
[g]Physics and Astronomy Dept., University of New Mexico, Albuquerque, NM 87131, USA

ABSTRACT

Future large aperture telescopes and high contrast imaging systems will often include segment gaps, structural obscurations, along with outer edges which produce diffraction effects that are disadvantageous to high contrast imaging (e.g., for exoplanet detection) or continuous wavefront control across the optical aperture. We present an optimization strategy for several pupil segment topologies for next-generation telescope concepts. Wave propagation results based on diffraction-limited point spread function analyses using Fraunhofer diffraction theory are presented using the Python-based POPPY simulation tool.

Keywords: Exoplanet, High contrast, Large segmented mirrors, Pinwheel pupil, Diffraction effects, Telescope structures, Starlight suppression, Scattered light

1. INTRODUCTION

Exoplanets are among the most fascinating and mysterious objects in the universe. They challenge the concept that we are alone in the universe. The planets are much fainter than their host stars, making observations of the planets nearly impossible. To circumvent this, astronomers have successfully developed several methods in the last two decades, including direct imaging, radial velocity, astrometry, gravitational microlensing, and transit photometry to detect and characterize exoplanets.[1]

As of this date[2], there are 4,266 confirmed planets in 3,152 systems, including 698 systems that have more than one known planet. However, direct imaging of exoplanets is ultimately essential for astronomers to obtain detailed spectra of a planet's surface and atmosphere. This is the best way to characterize planetary evolutionary tracks and estimate the size, temperature, and existence of liquid water. The existence of liquid water defines the habitable zone, which is the orbital region where life could be supported on an exoplanet. This zone is shown by the shaded region in Figure 1.[3] The inner and outer boundaries change accordingly with the size of the main-sequence star, the larger the star is, the farther the boundaries are.

Although we know the size of the habitable zone as a function of stellar mass (Figure 1), there are two challenging problems to conquer when directly imaging exoplanets with either a space telescope or a ground-based telescope. The first one is the angular separation of the parent star and the exoplanet. To understand why this angular separation plays a role in direct imaging, we consider imaging an earth-like extrasolar system. Table. 1 tabulates the distance to this Earth-like exoplanet, which has the same orbital distance from a Sun-like star as the Earth (1 AU). Column 2 shows the angular separation between the parent star and the planet, with the telescope centered on the star. Column 3

---

[*] letter2dwk@hotmail.com

calculates the telescope aperture diameter to resolve the angular separation while meeting the Rayleigh Criterion. Column 4 shows the telescope aperture needed to locate the image of exoplanet at the third dark ring of Airy Disk formed by the host star.
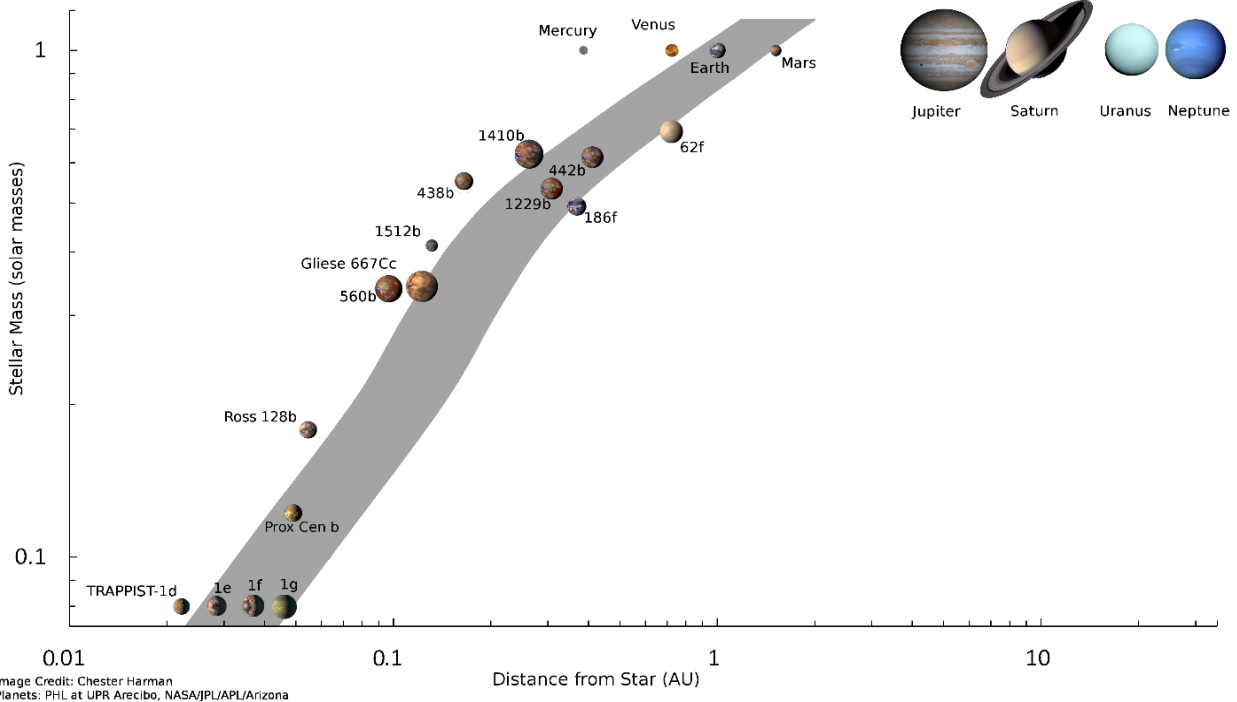
Figure 1: Diagram of habitable zone ranges and boundaries in log distance for main-sequence stars with zero-age. When a star lies along a curve on the Hertzsprung–Russell diagram with the dominant energy production process of nuclear fusion and having lost the excess energy obtained from gravitational contraction[4], then the star can be referred to "zero-age main-sequence[5,6]" stage. The stellar mass in the y-axis is the ratio comparing to the mass of our sun. (Image credit: Chester Harman; planet images from PHL@Arecibo; NASA/JPL).[7]

The second challenge is the irradiance collection. Considering the molecular band absorption of Earth's atmosphere, without other non-blackbody phenomena, the preferred wavelength reflectance ranges providing the evidence of life-supporting environment are $0.3 - 2.4$ μm in the visible to near-IR. Rayleigh scattering, which is important in the blue portion of the spectrum shortward of 450 to 500 nm, and vegetation reflection are most significant.[8–11] Traub and Jucks from Smithsonian Astrophysics Observatory (SAO), calculated a model of spectra from the whole Solar System at a distance of 10 PC.[12] The result showed that the ratio of flux arriving from the Earth-analogue to that of the Sun is about 10^{-10} in the visible to near-IR and about 10^{-6} in the mid-IR. The flux from an exoplanet is much fainter than that of its parent star and is easily polluted by the black-body continuum and the spectrum of the star. The calculation shown in Table 1 show that larger apertures are needed to provide high angular resolution and enough radiation-gathering ability to distinguish the spectrum of the exoplanet from its host star.

Table 1: Aperture Size required to resolve a distant exoplanet next to its host star for various distances and angles

Distance (Parsecs, PC)	Angle (milli-arcsec)	Aperture (m) in Rayleigh Criteria$^\Theta$	Aperture (m) in 3rd Ring$^\Theta$
10	100.0	2.52	7.63
20	50.0	5.03	15.3
30	33.3	7.55	22.9
40	25.0	10.1	30.5
50	20.0	12.6	38.2

$^\Theta$ Calculated for $\lambda = 1$μm.

2. LARGE TELESCOPE APERTURE SEGMENTATION TOPOLOGY

2.1 Today's aperture segment topology

During the 1980s, Dr. Jerry Nelson at the Lawrence Berkeley National Laboratory and the University of California presented the idea of using segmented mirrors for the Keck telescopes.[13] He developed the concept and necessary technologies to precisely shape the wavefront using computer-controlled adaptive optics with actuators and active alignment for the telescope mirror segments. Around 2000, several new telescopes with primary mirror sizes over 5-m began to appear. Today, several telescopes with 4 to 10 times larger than an effective aperture of 5-meters are under construction, including the European Extremely Large Telescope (ELT), the Thirty Meter Telescope (TMT), and the Giant Magellan Telescope (GMT), which are shown with others in Figure 2.
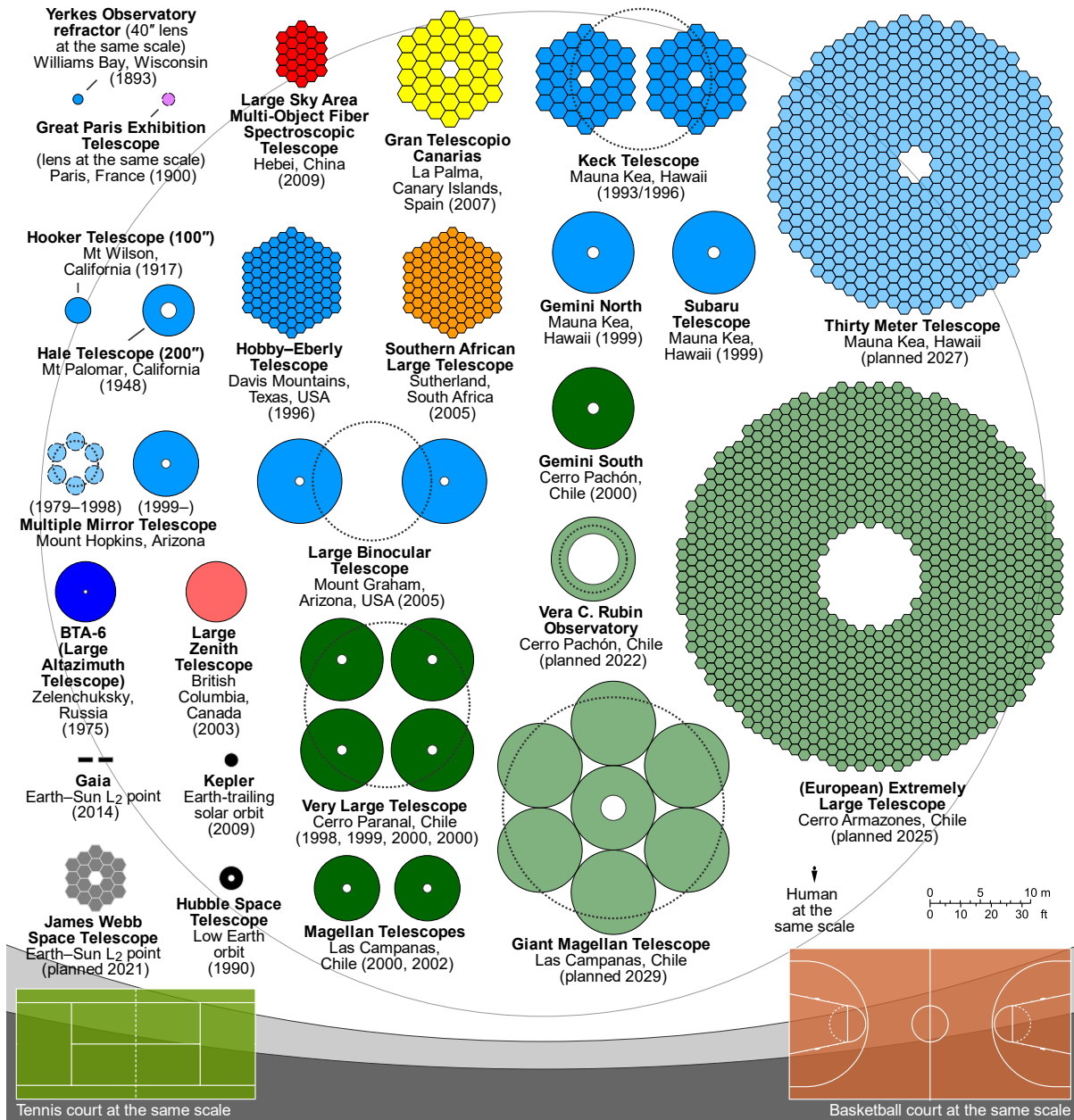

Figure 2: Comparison of nominal sizes and designs of primary mirrors or lenses of some famous optical telescopes. Note that the doted lines show the envelop of the equivalent radiation-gathering area of the combination mirrors.[14]

The concept of mirror segmentation has since spread worldwide and almost all future large optical telescopes are designed and constructed in this way.[15] Segmented design provide us with large enough effective apertures to achieve much higher angular resolution and light gathering power than previous telescopes.

The critical questions are how we design the topology of the segment shape to optimize the telescope performance for its measurement objective. The angular resolution of a telescope with a circular shaped primary mirror is independent of position angle at the field of view and therefore is optimum for most astronomy applications. There are many ways to partition a circular shaped primary mirror of a telescope in many segments. Examples are: circular/annual, hexagonal, pie shape, keystone. Also, the image performance of these segmented pupils has been comprehensively studied by many authors.[16–20] Many creative ways of segmentation have been suggested.[19,21–23] After several years of study, three topologies for large aperture primary mirrors have evolved. These are shown in Fig 2. They are: circular monolithic, circular segments, and hexagonal mirrors mosaiced with hexagonal segments.

Therefore, several surveys or papers about segmented mirror design are presented, including segmented coronagraph design and analysis (SCDA) study led by Stuart Shaklan (NASA Jet Propulsion Laboratory, JPL) and supported by NASA's Exoplanet Exploration Program (ExEP),[24] to provide efficient coronagraph design concepts for exoplanet imaging with future segmented aperture space telescopes.[25] The Caltech/JPL SCDA team first studied the combinations of 7 segmented aperture architectures and 6 obscuration architectures and compare their relative merits for segmentation, backplane configuration, stability, launch complexity, and secondary mirror support[26] Later, a detailed study considering the whole coronagraph instrument system, was published. Sensitivity and performance between different combinations of segmented pupils, apodizer, focal plane mask, and Lyot stop was carefully analyzed.[27] The SCDA did not cover and investigate telescope topologies other than those based on LUVOIR which were limited to hexagonal mirrors, mosaiced with hexagonal segments.

This manuscript will describe an independently developed segment architecture (not shown in Fig. 2) which 1) minimized diffraction confusion, 2) increases transmittance, and 3) lowers manufacturing complexity and corresponding costs.[22,23] Descriptive names for this innovative topology are the pinwheel aperture and pinwheel pupil segmentation.

2.2 Pinwheel pupil segmentation

The 6.5-m James Webb Space Telescope (JWST) and future planned large aperture space telescopes, such as LUVOIR A and LUVOIR B use arrays of hexagonally shaped mirrors deployed from the space-craft to fill or "tile" the doubly curved concave surface primary mirror. This mechanical deployment along with the imperfect optical surface figure accuracy near the edge results in gaps (or effective gaps) between segments. That is, the reflecting mirror surface is discontinuous.

Curved-sided segments are used to control image plane diffraction confusion. Werenskiold (1941)[28] was one of the first astronomers who documented that curved telescope secondary mirror spiders can improve planetary observation. Couder (1952)[29] described a form of a spider, formed by four spindle-shaped struts, which had an outline shaped by arcs of circles. The spindle shape struts could eliminate the spikes from stellar images that would otherwise subtle details on the surface and atmospheres of planets. Everhart and J. Kantorski (1959)[30] obtained spread-out diffraction patterns for the various curved strut. Richter (1984) provided a detailed Fraunhofer diffraction calculation and proved that a narrow crescent obscuration in the pupil plane can fan out the flares caused by the straight obscurations, which was called "obtuse angle searchlight effect" by him.[31]

Harvey and Ftaclas (1995) showed that secondary mirror spiders have diffraction effects that can degrade telescope image quality with different criteria.[32] Scalar diffraction theory and Fourier techniques were applied to predict the Strehl ratio, fractional encircled energy (FEE), and the modulation transfer function (MTF), with the parameters of central obscuration ratio, the particular spider configuration and the width of the spiders. A simple empirical equation was presented to accurately predict FEE performance for arbitrary central obscuration and spider configuration.

In 2016 Breckinridge observed that the hexagonal segment topology places three diffraction gratings across the aperture. These gratings create artifacts at the image plane that confuse the presence of exoplanets with the fixed pattern noise characteristic of grating diffraction. Based on his several years' experience as an amateur telescope maker and observer Breckinridge knew that amateur astronomers used curved struts on their Cassegrain and Newtonian secondary support structures to control diffraction to observe low contrast details on planetary surfaces. He investigated the possibility of using nesting segments whose gaps are curve sided to tile a large aperture primary

mirror. The preliminary numerical calculation provided digital evidence that curving the segment gaps would lead to controlling diffraction in a manner optimum for exoplanet science.

To not add further spatial structure to the diffraction pattern at the image plane that is already present from the curvature of the pupil edge, Breckinridge suggested that the radii of curvature of the gaps be the same as the radius of curvature of the pupil edge. These investigations were summarized in a poster paper presented at the 231st meeting of the American Astronomical Society (Jan 2018).[33] He proposed that NASA use a pinwheel aperture for LUVOIR A/B and future large aperture astrophysics telescopes that benefit from a point symmetric PSF.

Based on previous work, Harvey and Breckinridge (2018)[21] proposed a 3 Tier Pie wedge 12 Pinwheel Pupil concept and modeled the diffraction effects of it, which are devoid of any discrete narrow diffraction flares with substantial interference. The azimuthal irradiance profile of 5th, 10th, 15th, and 20th rings exhibit almost sinusoidal variation with 12 cycles. In the same year, Breckinridge and Harvey further illustrate the high possibility of manufacturing a curve-sided segment, using mirror substrates, processing steps, and polishing methods that are all available with currently existing technology.[22] In 2019, Breckinridge indicated a hex segmented aperture may produce Point Spread Function (PSF) that has many false-positive identifications of exoplanets, which may mask an actual exoplanet.[23]

3. WAVE PROPAGATION THROUGH SEGEMENTED OPTICS

3.1 Physical optics propagation using the `POPPY` software package

Physical Optics Propagation in Python (`POPPY`) [34], is a Python library primarily developed by a team of astronomers at the Space Telescope Science Institute and is open to contributions from scientists and software developers around the world. `POPPY` simulates physical optical propagation, including diffraction effects. With a flexible framework for modeling Fraunhofer[35] and Fresnel[36] diffraction and PSF calculations, especially in the context of astronomical telescopes, `POPPY` is used for various pupil topology investigation as shown in Figure 3, 4, and 5. Please, note that `POPPY` propagates the complex electromagnetic wavefront between planes using either the Fraunhofer or Fresnel approximations of scalar electromagnetic theory for monochromatic and/or polychromatic point spread functions through the analyzed optical system. It does not simulate vector electromagnetic field propagation (e.g., modeling polarization effects), which is not a limiting factor for the simulation study presented here. The development can be found on Github (http://github.com/spacetelescope/poppy) with the most current version.

`POPPY` was originally developed as part of a simulation package for JWST, which is a hexagonally segmented telescope. However, for our case study, we need to add some new software modules (classes) to fit our goal. New `POPPY` mask classes defined in Python were developed to create various types of structured pupils (e.g., Pinwheel pupil in Figure 3). To make PSFs of these pupils comparable, a number of parameters are set to a fixed value as follows.
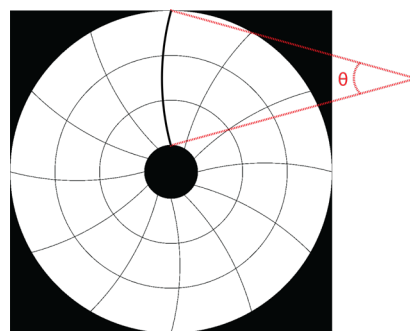

Figure 3: Illustration of the geometry of a Pinwheel pupil. θ is defined as the arc angle of a spoke.

All of the pupil topologies investigated in this study have the same outside diameter, D=12m; the same 3 off-axis layers (i.e., looks like annular rings for the case d and g – l in Fig. 4), same gap size (gap=0.02m), and the same number of 12 spokes in total (n_{spokes}, if there are any spokes). The central obscuration ratio, ε, indicates the ratio of the central obscuration to the diameter of a pupil (for Figure 4b – l). The flat to flat value, $f2f$, indicates the distance from one flat side to the other flat side of each segment showing in Figure 3e and indicates the diameter of each circle segment showing in Figure 4f.
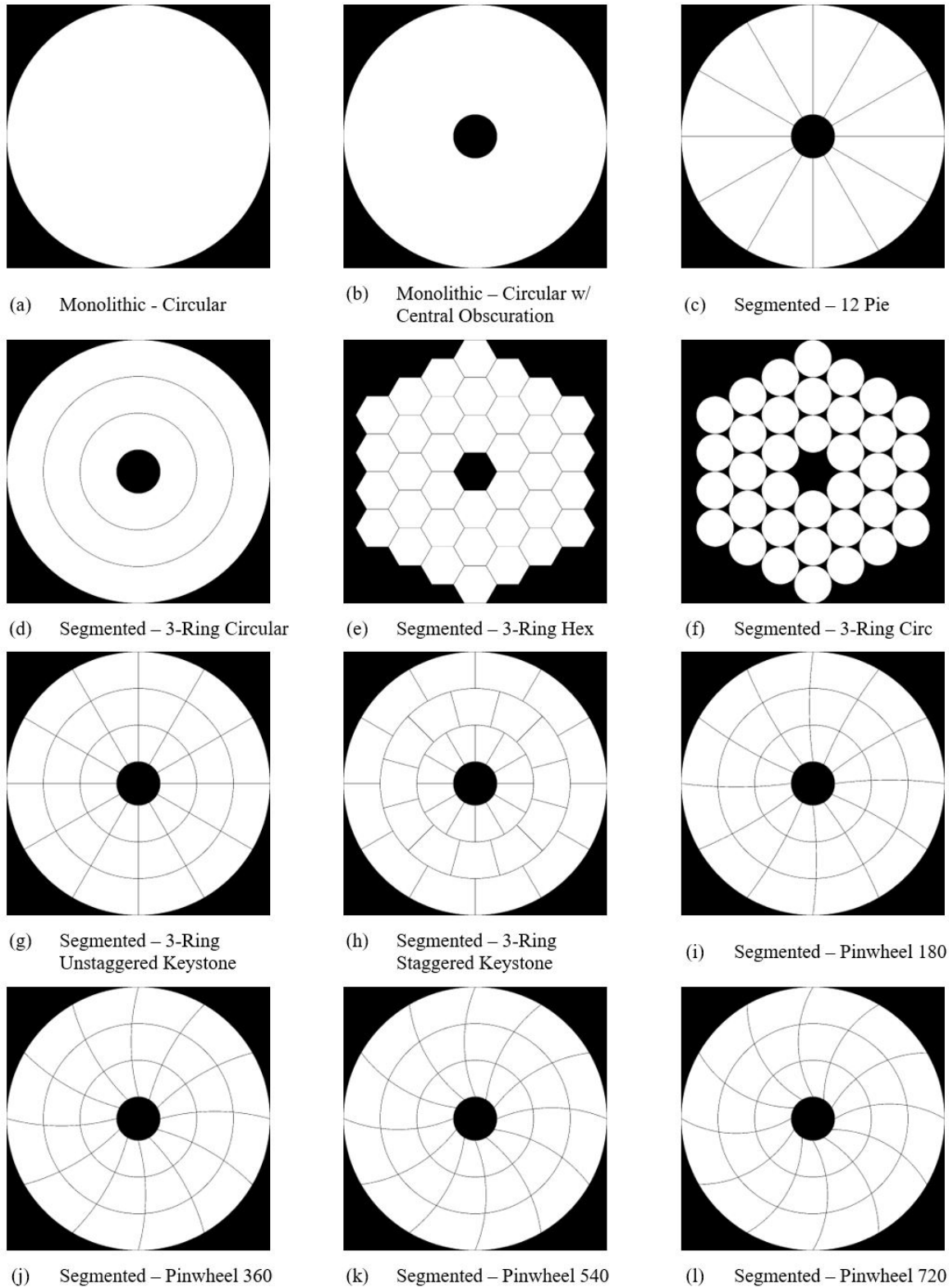
Figure 4: Illustration of the segmented pupil topologies investigated in this study. Each pupil has the same aperture diameter of 12 m. The white is the mirror's reflecting surface, and black shows the obscured area (Note: segment gap width is set to 20 mm). (Please, watch the Media 1 for the topological pupil variations.)
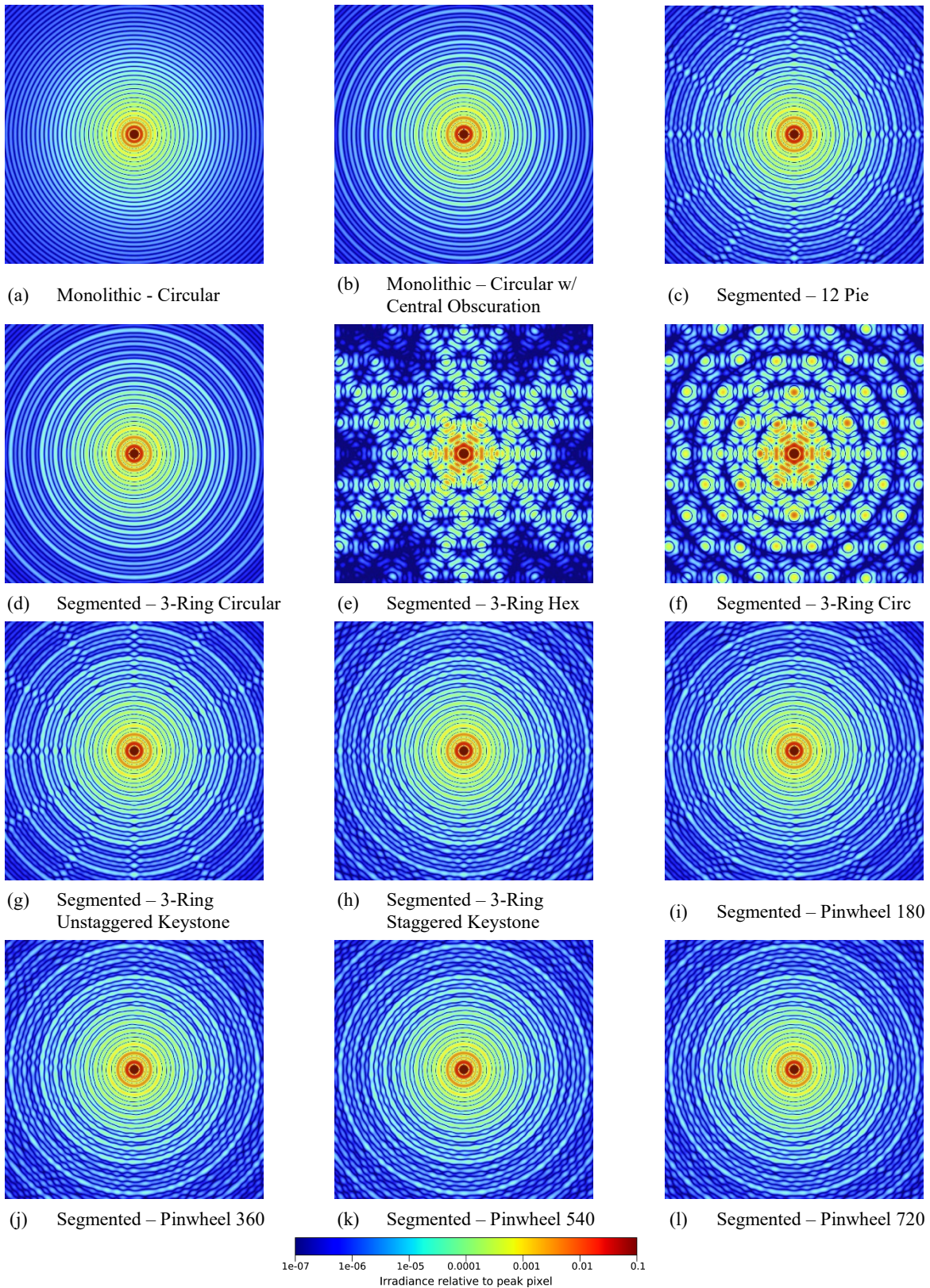
(a)   Monolithic - Circular

(b)   Monolithic – Circular w/ Central Obscuration

(c)   Segmented – 12 Pie

(d)   Segmented – 3-Ring Circular

(e)   Segmented – 3-Ring Hex

(f)   Segmented – 3-Ring Circ

(g)   Segmented – 3-Ring Unstaggered Keystone

(h)   Segmented – 3-Ring Staggered Keystone

(i)   Segmented – Pinwheel 180

(j)   Segmented – Pinwheel 360

(k)   Segmented – Pinwheel 540

(l)   Segmented – Pinwheel 720

Irradiance relative to peak pixel

Figure 5: Illustration PSFs within 1 arcsec field of view for each of the pupils listed in Figure 4, calculated at wavelength 1μm. The PSFs are all in log scale with color bar at the bottom indicated the value. (Please, watch the Media 1 for the PSF variations.)

The central obscuration used in Figure 4e is defined as the length of the corner to corner of a hexagonal segment with periphery gap, which is $(f2f + 2gap)/\cos 30°$. By drawing an inscribed circle in each hexagonal segment in Figure 4e, the pupil of Figure 4f can be obtained so the central obscuration of Figure 4f is calculated as $(f2f + 2gap)$. Due to the geometrical shape difference between a circle and hexagon, Figure 4e and 4f has different central obscuration. Applying the central obscuration value of Figure 4e to other pupils (Figure 4b – d and 4g – l), the central obscuration ratio of every pupil now shares the same ~0.17 value (i.e., $\varepsilon = ((f2f + 2gap)/\cos 30°)/D = ((f2f + 2gap)/\cos 30°)/12 \approx 0.1672$), except Figure 4f, which has ~0.14 obscuration ratio (i.e., $\varepsilon = (f2f + 2gap)/D = (f2f + 2gap)/12 \approx 0.1448$).

The arc geometry of the combination of every spoke in a "Pinwheel" pupil is controlled by Total Spokes Angle, which needs to be the integer multiple of 180° in order to have a bow-tie effect on PSFs.[22,31] The Total Spokes Angle is defined as

$$Total\ Spokes\ Angle\ (TSA) = n_{spokes} \times \theta \qquad (1)$$

, where n_{spokes} is the total spokes number in a Pinwheel pupil and θ is the arc angle of a spoke (Figure 3). The Total Spokes Angle of Pinwheel pupils showing from Figure 4i to Figure 4l is 180°, 360°, 540°, and 720°, respectively. Note that every gap or spoke can be regarded as a spider strut or just purely a gap between segmented mirrors.

3.2 Diffraction-limited point spread function simulation

The diffraction-limited PSF of each pupil is calculated using POPPY and shown in Figure 5, with wavelength 1μm and the PSF plots are all normalized to one at the central peak. Figure 5a is the Airy Disk irradiance pattern from a circular pupil. As the pupil is sliced into different segment topology, the shape of the PSF varies and changes rapidly as shown in Media 1.

By simple observation, we can already tell that Figure 5a is the Airy pattern, and Figure 5b has a slightly different irradiance distribution from ring to ring because of the spatial frequencies of the outer aperture beating against those caused by the inner aperture.

When some numbers of radial direction spokes are added on the pupil plane, the irradiance of every ring appears some "peaks" along the azimuthal direction in Figure 5c, corresponding to 12 spokes (and their associated edge diffraction for the gaps) in the pupil plane. For 3-Ring Hex and Circ, because of the different grating-like period from the repeating gaps in different directions of the pupil plane, different flares in different directions create many fake stars/exoplanets images spreading in image plane.[22]

4. POINT SPREAD FUNCTION ANALYSIS

Fractional encircled energy (FEE) is an important criterion to determine image quality, especially, for astronomical applications. Figure 6 illustrates the 2-dimensional FEE simulation results of all pupil cases in Figure 5. If the segmented configuration at the pupil plane is radially symmetric (e.g., Circular with Central Obscuration and 3-Ring Circular) the FEE plot then has better performance with approaching the curve of the Circular pupil. When the pupil plane contains radially-structured spokes, (e.g., Pinwheel 180 or 360 pupils) FEE plots start to experience different degrees of degradation. In our parameter space, 12 Pie has better FEE performance comparing to others with radially structured pupils. Also, for the Pinwheel mirror aperture, the Total Spokes Angle has almost no impact on the FEE performance (Figure 6).

Focusing on the 3-Ring Hex pupil and Pinwheel180 pupil, we report the azimuthally averaged radial profiles in Figure 7. The 3-Ring Hex pupil is a popular mirror among current telescopes (e.g., Keck I & II), whereas the Pinwheel 180 is a new concept reported by Harvey and Breckinridge[22]. Irradiance is plotted in a log scale, and the averaged profiles are drawn in thick black solid lines, the logarithmic error bars, calculated with one standard deviation, are represented by the red region.[37] The maximum (i.e., flare-like brightest local spot) and minimum (i.e., darkest local spot) of the irradiance values in a given radius circle (in arcsec) are continuously plotted from 0 arcsec to about 0.7 arcsec, in blue solid lines.

In Figure 7, the azimuthally averaged PSF of 3-Ring Hex has several characteristic local dark zones including the two local minima at 0.14 arcsec and 0.365 arcsec. If astronomers know where an exoplanet located, they can rotate (i.e., boresight roll) the whole large hex-segmented telescope spacecraft to cause the exoplanet's image fall on that local

minimum ring caused by that of the host star to analyze the spectrum of the exoplanet. In this way, the "flares", "spikes" or "fake exoplanet image" caused by host stars that are seen through the "segment edge diffraction grating" across the aperture can be circumvented, and thus obtain a less polluted exoplanet image.
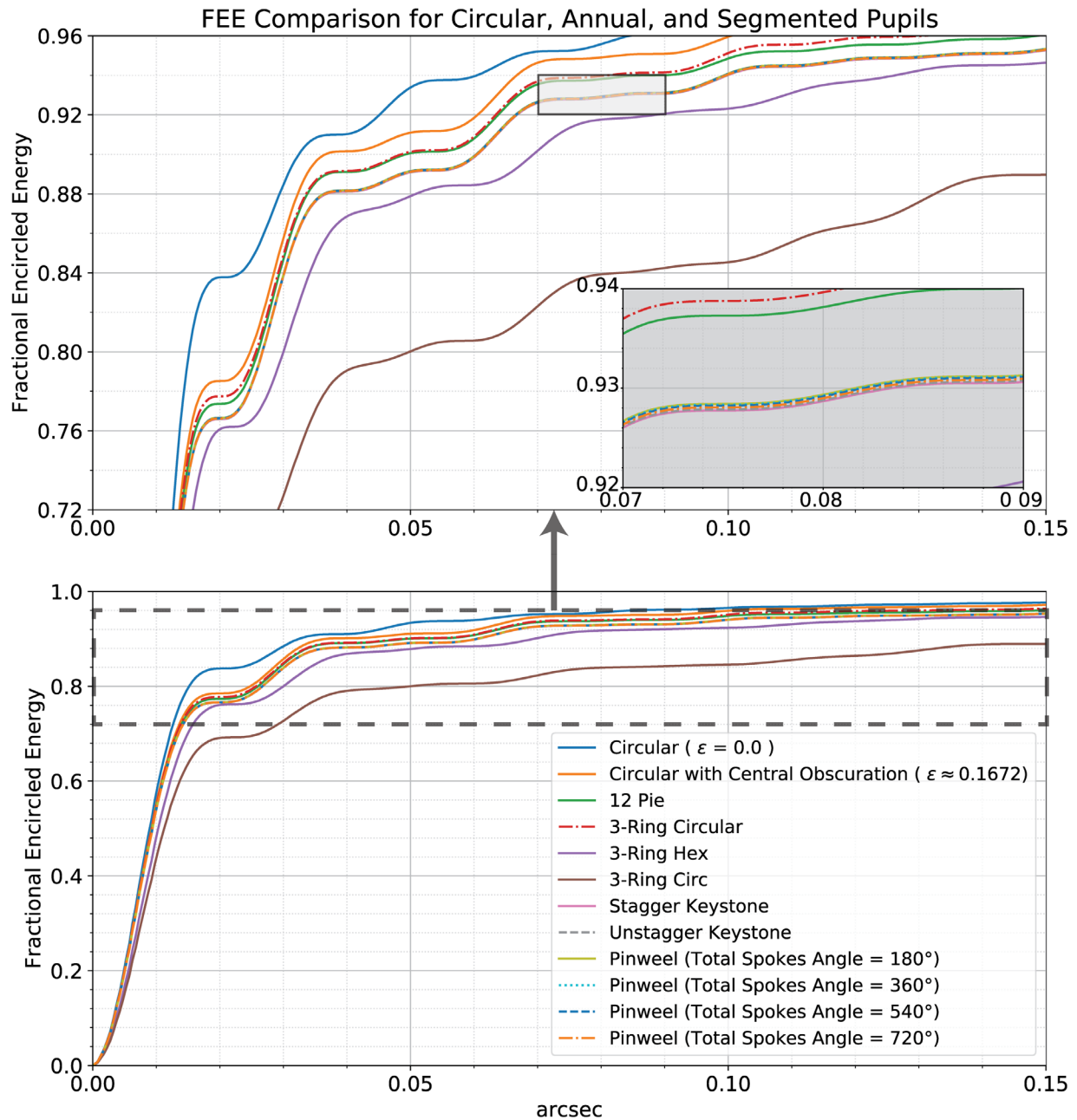

Figure 6: Fractional Encircled Energy (FEE) of 12 Pupils' 2-dimensional PSFs in Figure 5. The FEE curves of Pinwheel 180, Pinwheel 360, Pinwheel 540, and Pinwheel 720 shows almost the same performance. The (top) plot shows the zoom-in section for the FEE range between 0.72 – 0.96 of the (bottom) plot. The grey box is a further zoom-in section for the FEE range between 0.92 – 0.94 of the (bottom) plot.

However, the radial profile has about 10^2 power of relative standard deviation along the azimuthal direction, which indicates that the irradiance within one ring has a large variation. Such fluctuation may cause more sensitivity and

noise management issues during a searching exo-planet observation mode requiring an azimuthal averaging during a long exposure time. Moreover, the maximum and minimum profile range is quite large, spanning from 10^{-17} to 10^{-6}, indicating that careful alignment and positioning of the unresolved exoplanet (only if the exoplanet's location is already known) is highly required while operating the telescope system.

In contrast, applying a pinwheel pupil design to a future telescope may complement the hexagonal segmentation case with the advantages of reducing the extreme spikes and the azimuthal variation of the irradiance pattern in the PSF, decreasing confusion caused by mid-spatial frequency speckles.
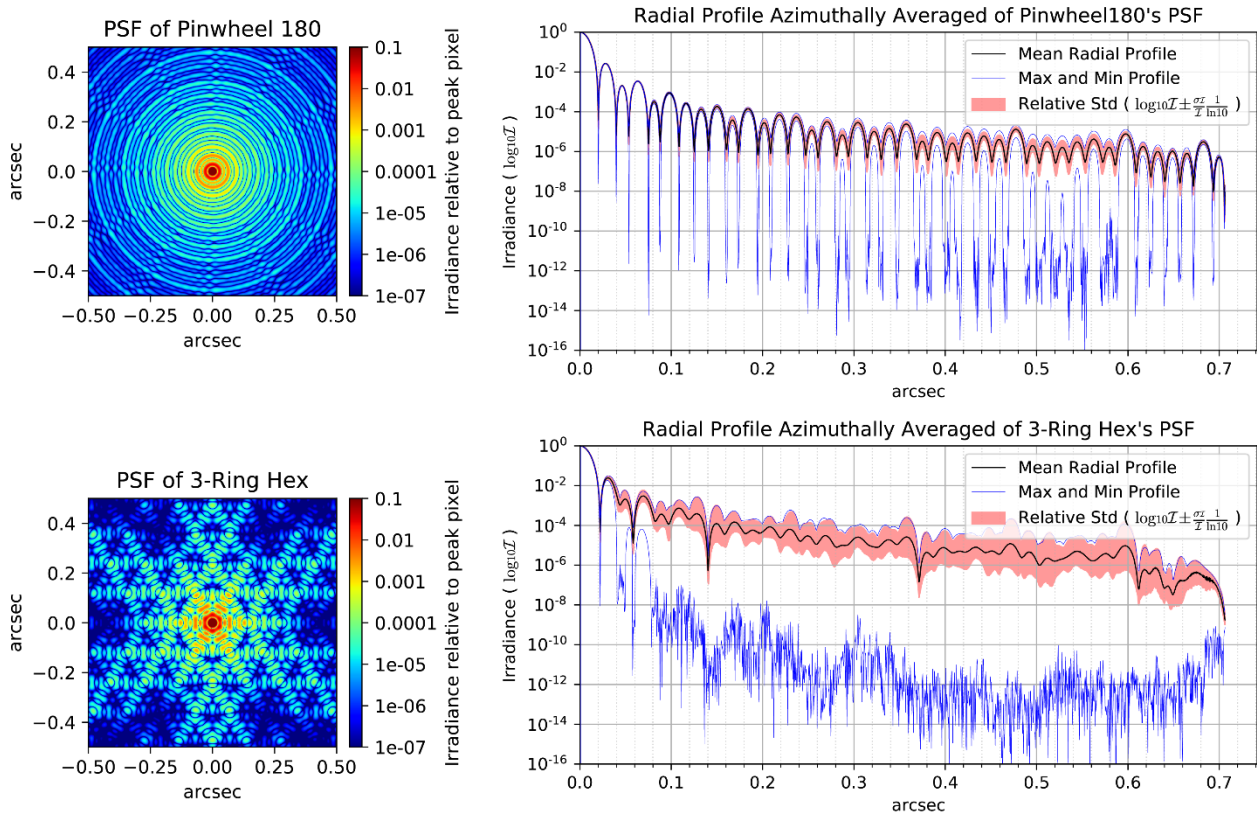

Figure 7: The PSF (at the prime focal plane) comparison between the Pinwheel 180 (top) and the 3-Ring Hex (bottom) for 12 m full aperture size at monochromatic 1 μm wavelength as described in Figure 4 and 5. Irradiance is plotted in a log scale, and the averaged profiles are drawn in thick black solid lines, the logarithmic error bars, calculated with one standard deviation, are represented by the red region.26 The maximum (i.e., brightest fake spot) and minimum (i.e., deepest dark zone) of the irradiance values in a given radius circle (in arcsec) are continuously plotted from 0 arcsec to about 0.7 arcsec, in blue solid lines.

Of course, all these factors need to be considered along with the rest of a specific telescope/instrument configuration such as secondary mirror spider structure and coronagraph approach, e.g., a coronagraph optimized for the specific pupil. The presented results are not to compare the performance between specific pupils, but rather to point out different characteristics and pros-and-cons of each pupil to use as a concept or a reference for future use.

5. CONCLUDING REMARKS

Fractional encircled energy (FEE) and azimuthally averaged radial profile of point spread functions corresponding to various telescope pupils are analyzed. Modern segmented mirror designs have been mostly hexagonal or circular, but we explore more options for future telescopes. A hex-segmented pupil has much higher irradiance spikes but also appears to have significant regions of lower irradiance. Pinwheel pupil doesn't have such a min-max region but provides more uniform irradiance distribution both in the bright rings and the dark rings of PSF, which could improve the performance of active wavefront control for exoplanet imaging and decrease confusion in crowded astronomical fields such as star clusters.

The fundamental and important topological analysis presented in this paper is expected to provide a guideline for next-generation telescope primary mirror segmentation and secondary spider design. Furthermore, we added new classes to the open-access software package POPPY to represent these novel primary mirror concepts.

The performance of a pinwheel aperture integrated to a "typical" vector vortex coronagraph (e.g., VV6 or VV8) system like that investigated for HabEx, remains to be evaluated. Intuitively, the advantage of using a pinwheel pupil with a coronagraph offers very significant gains for the detailed spectral characterization of terrestrial exoplanets for atmospheric composition, geology, evolution, and probability for life.

ACKNOWLEDGEMENT

REFERENCES

[1]   Wright, J. T.; Gaudi, B. S. Exoplanet Detection Methods. arXiv:1210.2471 [astro-ph] 2012. https://doi.org/10.1007/978-90-481-8818-5_59.

[2]   Schneider, J. The Extrasolar Planets Encyclopaedia http://exoplanet.eu/ (accessed May 15, 2020).

[3]   Kopparapu, R. K.; Ramirez, R.; Kasting, J. F.; Eymet, V.; Robinson, T. D.; Mahadevan, S.; Terrien, R. C.; Domagal-Goldman, S.; Meadows, V.; Deshpande, R. Habitable Zones around Main-Sequence Stars: New Estimates. The Astrophysical Journal 2013, 765, 131. https://doi.org/10.1088/0004-637X/765/2/131.

[4]   Schilling, G. New Model Shows Sun Was a Hot Young Star. Science 2001, 293 (5538), 2188–2189. https://doi.org/10.1126/science.293.5538.2188.

[5]   Zero Age Main Sequence | COSMOS https://astronomy.swin.edu.au/cosmos/Z/Zero+Age+Main+Sequence (accessed May 26, 2020).

[6]   Hansen, C. J.; Kawaler, S. D. Stellar Interiors: Physical Principles, Structure, and Evolution; Springer Science & Business Media, 1999.

[7]   Kasting, J. F.; Kopparapu, R.; Ramirez, R. M.; Harman, C. E. Remote Life-Detection Criteria, Habitable Zone Boundaries, and the Frequency of Earth-like Planets around M and Late K Stars. Proceedings of the National Academy of Sciences 2014, 111 (35), 12641–12646. https://doi.org/10.1073/pnas.1309107110.

[8]   Turnbull, M. C.; Traub, W. A.; Jucks, K. W.; Woolf, N. J.; Meyer, M. R.; Gorlova, N.; Skrutskie, M. F.; Wilson, J. C. Spectrum of a Habitable World: Earthshine in the Near-Infrared. The Astrophysical Journal 2006, 644, 551–559. https://doi.org/10.1086/503322.

[9]   Robinson, T. D.; Meadows, V. S.; Crisp, D.; Deming, D.; A'Hearn, M. F.; Charbonneau, D.; Livengood, T. A.; Seager, S.; Barry, R. K.; Hearty, T.; Hewagama, T.; Lisse, C. M.; McFadden, L. A.; Wellnitz, D. D. Earth as an Extrasolar Planet: Earth Model Validation Using EPOXI Earth Observations. Astrobiology 2011, 11 (5), 393–408. https://doi.org/10.1089/ast.2011.0642.

[10]   Seager, S. What Could Aliens See, Looking at Earth from Afar? In Is There Life Out There? The Search for Habitable Exoplanets; 2009; p 10.

[11]   Seager, S. The Future of Spectroscopic Life Detection on Exoplanets. PNAS 2014, 111 (35), 12634–12640. https://doi.org/10.1073/pnas.1304213111.

[12]   Des Marais, D. J.; Harwit, M. O.; Jucks, K. W.; Kasting, J. F.; Lin, D. N. C.; Lunine, J. I.; Schneider, J.; Seager, S.; Traub, W. A.; Woolf, N. J. Remote Sensing of Planetary Properties and Biosignatures on Extrasolar Terrestrial Planets. Astrobiology 2002, 2 (2), 153–181. https://doi.org/10.1089/15311070260192246.

[13]   Nelson, J. Segmented Mirror Design For A 10-Meter Telescope. In Instrumentation in Astronomy III; International Society for Optics and Photonics, 1979; Vol. 0172, pp 31–38. https://doi.org/10.1117/12.957064.

[14]   Wikipedia, "Cmglee. English::Comparison optical telescope primary mirrors.svg," last modified 20 June 2020, https://commons.wikimedia.org/wiki/File:Comparison_optical_telescope_primary_mirrors.svg

[15]   Wikipedia, List of Largest Optical Reflecting Telescopes.; 2020.

[16]   Manhart, P. K.; Rodgers, J. M. Segmented Mirror, Manufacturing And Alignment Tolerances (SMMAT). In Active Telescope Systems; International Society for Optics and Photonics, 1989; Vol. 1114, pp 387–405. https://doi.org/10.1117/12.960843.

[17]   Yaitskova, N.; Dohlen, K. Tip–Tilt Error for Extremely Large Segmented Telescopes: Detailed Theoretical Point-Spread-Function Analysis and Numerical Simulation Results. J. Opt. Soc. Am. A, JOSAA 2002, 19 (7), 1274–1285. https://doi.org/10.1364/JOSAA.19.001274.

[18]   Yaitskova, N.; Dohlen, K.; Dierickx, P. Analytical Study of Diffraction Effects in Extremely Large Segmented Telescopes. J. Opt. Soc. Am. A, JOSAA 2003, 20 (8), 1563–1575. https://doi.org/10.1364/JOSAA.20.001563.

[19]   Lightsey, P. A.; Chrisp, M. Image Quality for Large Segmented Space Telescopes. In IR Space Telescopes and Instruments; International Society for Optics and Photonics, 2003; Vol. 4850, pp 453–460. https://doi.org/10.1117/12.461220.

[20]   Cornils, R.; Gillessen, S.; Jung, I.; Hofmann, W.; Beilicke, M.; Bernlöhr, K.; Carrol, O.; Elfahem, S.; Heinzelmann, G.; Hermann, G.; Horns, D.; Kankanyan, R.; Katona, A.; Krawczynski, H.; Panter, M.; Rayner, S.; Rowell, G.; Tluczykont, M.; van Staa, R. The Optical System of the H.E.S.S. Imaging Atmospheric Cherenkov Telescopes. Part II: Mirror Alignment and Point Spread Function. Astroparticle Physics 2003, 20 (2), 129–143. https://doi.org/10.1016/S0927-6505(03)00172-5.

[21]   Harvey, J. E.; Breckinridge, J. B.; Irvin, R. G.; Pfisterer, R. N. Novel Designs for Minimizing Diffraction Effects of Large Segmented Mirror Telescopes. In Current Developments in Lens Design and Optical Engineering XIX; International Society for Optics and Photonics, 2018; Vol. 10745, p 107450L. https://doi.org/10.1117/12.2326923.

[22]   Breckinridge, J. B.; Harvey, J. E.; Crabtree, K.; Hull, T. Exoplanet Telescope Diffracted Light Minimized: The Pinwheel-Pupil Solution. In Space Telescopes and Instrumentation 2018: Optical, Infrared, and Millimeter Wave; International Society for Optics and Photonics, 2018; Vol. 10698, p 106981P. https://doi.org/10.1117/12.2311811.

[23]   Breckinridge, J. B.; Harvey, J. E.; Irvin, R.; Chipman, R.; Kupinski, M.; Davis, J.; Kim, D.-W.; Douglas, E.; Lillie, C. F.; Hull, T. ExoPlanet Optics: Conceptual Design Processes for Stealth Telescopes. In UV/Optical/IR Space Telescopes and Instruments: Innovative Technologies and Concepts IX; International Society for Optics and Photonics, 2019; Vol. 11115, p 111150H. https://doi.org/10.1117/12.2528825.

[24]   Exoplanet Program: Segmented Coronagraph Design and Analysis (SCDA) https://exoplanets.nasa.gov/exep/technology/SCDA (accessed May 7, 2020).

[25]   Shaklan, S. Segmented Coronagraph Design and Analysis (SCDA) A Study by the Exoplanet Exploration Program. 36.

[26]   Feinberg, L.; Hull, T.; Krist, J.; Lightsey, P.; Matthews, G.; Shaklan, S.; Stahl, H. P. Apertures for Segmented Coronagraph Design and Analysis. 23.

[27]   Ruane, G.; Jewell, J.; Mawet, D.; Shaklan, S.; Stark, C. C. Segmented Coronagraph Design and Analysis (SCDA): An Initial Design Study of Apodized Vortex Coronagraphs. arXiv:1712.02042 [astro-ph, physics:physics] 2017.

[28]   Werenskiold, C. H. Improved Telescope Spider Design. Journal of the Royal Astronomical Society of Canada 1941, 35, 268.

[29]   Couder, A. Dealing with Spider Diffraction. In Amatuer Telescope Making Advanced (Book Two) A Sequiel to Amateur Telescope Making (Book One); Ingalls, A. G., Ed.; Scientific American, Inc.: Kingsport, Tennessee, United States of America, 1952; Vol. 650, pp 620–622.

[30]   Everhart, E.; Kantorski, J. W. Diffraction Patterns Produced by Obstructions in Reflecting Telescopes of Modest Size. The Astronomical Journal 1959, 64, 455. https://doi.org/10.1086/107973.

[31]   Richter, J. L. Spider Diffraction: A Comparison of Curved and Straight Legs. Appl. Opt., AO 1984, 23 (12), 1907–1913. https://doi.org/10.1364/AO.23.001907.

[32]   Harvey, J. E.; Ftaclas, C. Diffraction Effects of Telescope Secondary Mirror Spiders on Various Image-Quality Criteria. Appl Opt 1995, 34 (28), 6337–6349.

[33]   Breckinridge, J. B. The pinwheel pupil discovery: exoplanet science & improved processing with segmented telescopes, Poster # 439.04 - American Astronomical Society 231st meeting, 12 Jan 2018 Washington DC.

[34]   Perrin, M.; Long, J.; Douglas, E.; Sivaramakrishnan, A.; Slocum, C.; others. POPPY: Physical Optics Propagation in PYthon. Astrophysics Source Code Library 2016, ascl:1602.018.

[35]   Perrin, M. D.; Soummer, R.; Elliott, E. M.; Lallo, M. D.; Sivaramakrishnan, A. Simulating Point Spread Functions for the James Webb Space Telescope with WebbPSF. In Space Telescopes and Instrumentation 2012: Optical, Infrared, and Millimeter Wave; International Society for Optics and Photonics, 2012; Vol. 8442, p 84423D. https://doi.org/10.1117/12.925230.

[36]   Douglas, E. S.; Perrin, M. D. Accelerated Modeling of near and Far-Field Diffraction for Coronagraphic Optical Systems. In Space Telescopes and Instrumentation 2018: Optical, Infrared, and Millimeter Wave; International Society for Optics and Photonics, 2018; Vol. 10698, p 106982U. https://doi.org/10.1117/12.2313441.

[37]   Baird, D. C. The Propagation of Uncertainnties. In Experimentation: An Introduction to Measurement Theory and Experiment Design; Prentice-Hall: Englewood Cliffs, New Jersey, 1962; pp 48–74.